GEOPHYSICS, VOL. 62, NO. 6 (NOVEMBER-DECEMBER 1997); P. 1758–1773, 14 FIGS.

Ground-penetrating radar velocity tomography in heterogeneous and anisotropic media

Don W. Vasco*, John E. Peterson, Jr.*, and Ki Ha Lee‡

ABSTRACT

A ray series solution for Maxwell's equations provides an efficient numerical technique for calculating wavefronts and raypaths associated with electromagnetic waves in anisotropic media. Using this methodology and assuming weak anisotropy, we show that a perturbation of the anisotropic structure may be related linearly to a variation in the traveltime of an electromagnetic wave. Thus, it is possible to infer lateral variations in the dielectric permittivity and magnetic permeability matrices. The perturbation approach is used to analyze a series of crosswell ground-penetrating radar surveys conducted at the Idaho National Engineering Laboratory. Several important geological features are imaged, including a rubble zone at the interface between two basalt flows. Linear low-velocity anomalies are imaged clearly and are continuous across well pairs.

INTRODUCTION

Compared with other technologies, ground-penetrating radar (GPR) is a relatively new geophysical exploration tool. Despite its recent appearance, it has been applied to numerous engineering and geotechnical problems (Steward and Unterberger, 1976; Ulriksen, 1982; Olsson et al., 1987; Daniels, 1988; Davis and Annan, 1989). In specific environments, for example, hard-rock sites, GPR has proven economical and effective. Its resolution is sufficiently high to locate buried objects in archaeological investigations (Bevan, 1991).

In many respects, the analysis of GPR data parallels seismic data reduction and interpretation. For example, GPR reflection data have been processed with a standard seismic processing sequence (Fisher et al., 1992), drawing on an analogy between electromagnetic and seismic wave propagation (Lee et al., 1987). Recently, ray-tracing algorithms similar to those used in seismology have been proposed for the interpretation of cross-borehole electromagnetic data (Lee and Xie, 1993; Nekut, 1994) as well as GPR data (Goodman, 1994).

In this paper, we examine electromagnetic wave propagation in slightly inhomogeneous and anisotropic geological structures. The importance of anisotropy in the propagation of seismic waves has been recognized for some time (Backus, 1962) and has been the subject of numerous investigations (Leary et al., 1990). Because the mechanisms that produce seismic anisotropy (layering, rock fabric, and preferred orientation of crystals) also operate on electromagnetic wavefields, they are likely to influence electromagnetic wave propagation. The directional dependence of electric properties has been documented in the earth (Al Hagrey, 1994; Tillard, 1994), and the anisotropy of crystals is discussed in many optics texts (Born and Wolf, 1970; Lipson and Lipson, 1981). Therefore, it is important to account for anisotropy in electromagnetic data, for example, in GPR traveltimes. We develop a perturbation approach to relate GPR traveltimes to weak velocity anisotropy. The resulting linearization forms the basis for an inversion scheme to determine lateral variations in anisotropic electromagnetic wave velocity from crosswell GPR traveltimes gathered at the Idaho National Engineering Laboratory (INEL).

METHODOLOGY

To relate GPR arrival times to the parameters of an anisotropic medium, we rely on an approach, presented in Kline and Kay (1965) and based on the university lectures of Luneburg (1966), that allows examination of the propagation of discontinuities in a time-varying vector field. This rigorous methodology, based on the ray-series expansion, is an important technique in seismology (Aki and Richards, 1980) but, to our knowledge, it is not used widely in the interpretation of electromagnetic data. For this reason, we present an outline of the approach in the Appendix, making our discussion more self-contained and easier to follow. The full treatment, as well as an extension to higher-order terms in the ray series, is given in Kline and Kay (1965).

Manuscript received by the Editor December 18, 1995; revised manuscript received October 28, 1996.
*Center for Computational Seismology, Berkeley Laboratory, Berkeley, California 94720. E-mail: dwvasco@lbl.gov and barstow@ccs.lbl.gov.
‡Earth Sciences Division, Berkeley Laboratory, Berkeley, California 94720. E-mail: khlee@lbl.gov.

Weak anisotropy and perturbed traveltimes

In this section, a perturbation technique is used to develop a relationship between small changes in the anisotropy parameters and a change in the calculated first-arrival time. The case of weak anisotropy has been studied extensively by seismologists (Backus, 1962; Berryman, 1979; Thomsen, 1986). Furthermore, several investigations have derived relationships between perturbations in anisotropy properties and seismic first-arrival times (Červený and Jech, 1982; Stewart, 1988; Jech and Pšenčík, 1989; Chapman and Pratt, 1992). In our derivations, the approach of Jech and Pšenčík (1989) and Chapman and Pratt (1992) is adapted for electromagnetic wave propagation within the earth.

From Maxwell's equations (see the Appendix), we may derive a linear relationship between the dielectric displacement vector $\mathbf{D}^*$ and the magnetic induction vector $\mathbf{B}^*$ for an anisotropic medium characterized by a spatially varying dielectric matrix (ϵ) and a magnetic permeability matrix (μ), written as

$$\begin{aligned} \mathbf{D}^* + (\epsilon)\mathbf{s} \times \mathbf{B}^* = 0, \\ (\mu)\mathbf{s} \times \mathbf{D}^* - \mathbf{B}^* = 0, \end{aligned} \tag{1}$$

where $\mathbf{s}$ is the ray tangent defined in the Appendix by equation (A-9). For these linear algebraic equations to have a nonzero solution, the determinant of the coefficient matrix must vanish, such that

$$\det(\epsilon_{jq}\mu_{ik}e_{k\ell j}e_{qnm}s_\ell s_n + \delta_{ij}\delta_{jm}) = 0, \tag{2}$$

where δ_{ij} denotes the Kroeneker delta, which is 1 for $i = j$ and 0 otherwise, and e_{ijk} denotes the pseudotensor, which is 1 under an even permutation of indices, -1 under an odd permutation of indices, and 0 for any repetition of indices (Sokolnikoff, 1964). Equation (2) may be written succinctly as

$$\det\left(a_{\ell imn}\hat{s}_\ell\hat{s}_n - \lambda^2\delta_{im}\right) = 0, \tag{3}$$

where

$$a_{\ell imn} = -\epsilon_{jq}\mu_{ik}e_{k\ell j}e_{qnm}, \tag{4}$$

$\hat{s}_\ell$ denotes the ℓth component of the unit vector in the direction of $\mathbf{s}$, and $\lambda = |\mathbf{s}|$.

Rather than applying perturbation methods directly to equations (3) and (4), we rewrite the system of equation (1) in a simpler form (Kline and Kay, 1965). Because the matrices (ϵ) and (μ) are real and symmetric, it is possible to factor them as

$$(\epsilon) = (\epsilon)_{1/2}(\epsilon)_{1/2} \tag{5}$$

and

$$(\mu) = (\mu)_{1/2}(\mu)_{1/2}, \tag{6}$$

where $(\epsilon)_{1/2}$ and $(\mu)_{1/2}$ are symmetric (Golub and Van Loan, 1989). We define a set of transformed vectors,

$$\begin{aligned} \mathbf{s}' &= \Delta^{1/2}(\mu)^{-1}_{1/2}\mathbf{s}, \\ \mathbf{D}' &= \Delta^{1/2}(\mu)^{-1}_{1/2}\mathbf{D}^*, \\ \mathbf{B}' &= \Delta^{1/2}(\mu)^{-1}_{1/2}\mathbf{B}^*, \end{aligned} \tag{7}$$

where Δ is the determinant of the matrix (μ). In the transformed coordinates, the system of equation (1) has the form

$$\begin{aligned} \mathbf{D}' + (\nu)\mathbf{s}' \times \mathbf{B}' = 0, \\ \mathbf{s}' \times \mathbf{D}' - \mathbf{B}' = 0, \end{aligned} \tag{8}$$

with (ν) being given by $(\mu)^{-1}_{1/2}(\epsilon)(\mu)^{-1}_{1/2}$. The system of equation (8) has a simpler form than that of equation (1). Consequently, the condition for its solution given by equations (3) and (4) also is simplified. Specifically, equation (4) now has the form

$$a_{\ell imn} = -\nu_{jq}e_{i\ell j}e_{qnm}. \tag{9}$$

Note that if the medium is nonmagnetic or only weakly magnetic, (μ) may be taken to be diagonal, with all elements being equal.

Now consider the effect of a perturbation in material properties, that is, a small change in $a_{\ell imn}$, which we denote by $\delta a_{\ell imn}$. As in Chapman and Pratt (1992), consider the eigenvector-eigenvalue equation associated with the system of equation (1),

$$\left(A_{im} - \lambda^2_{(j)}\delta_{im}\right)\Lambda^{(j)}_m = 0, \tag{10}$$

where $A_{im} = a_{\ell imn}\hat{s}_\ell\hat{s}_n$ and $\lambda_{(j)}$ and $\mathbf{\Lambda}^{(j)}$ denote the jth eigenvalue and eigenvector, respectively. A perturbation in $a_{\ell imn}$ induces perturbations in both $\lambda_{(j)}$ and $\mathbf{\Lambda}^{(j)}$, to first order, such that

$$\left(A_{im} - \lambda^2_{(j)}\delta_{im}\right)\delta\Lambda^{(j)}_m + \left(\delta A_{im} - 2\lambda_{(j)}\delta\lambda_{(j)}\delta_{im}\right)\Lambda^{(j)}_m = 0. \tag{11}$$

In general, for electromagnetic waves in an anisotropic medium, there are two waves propagating with distinct velocities (Born and Wolf, 1970; Lipson and Lipson, 1981). However, these velocities vary with direction and, in the most degenerate case, are equal for waves propagating in the four directions of the optical axes (Kline and Kay, 1965). Our analysis is along the lines of Chapman and Pratt (1992) and Jech and Pšenčík (1989). Consider two vector, $\mathbf{\Lambda}^{(2)}$ and $\mathbf{\Lambda}^{(3)}$, lying in the plane perpendicular to $\mathbf{\Lambda}^{(1)} = \mathbf{s}$. Such vectors may be written as

$$\begin{aligned} \Lambda^{(2)}_i &= r_{22}u^{(2)}_i + r_{23}u^{(3)}_i, \\ \Lambda^{(3)}_i &= r_{32}u^{(2)}_i + r_{33}u^{(3)}_i, \end{aligned} \tag{12}$$

where $\mathbf{u}^{(2)}$ and $\mathbf{u}^{(3)}$ are unit vectors perpendicular to $\mathbf{s} = \mathbf{u}^{(1)}$ and r_{ij} denote the components of a rotation matrix. As in Chapman and Pratt (1992), we may multiply the perturbation equation (11) with $j = 2$ by $u^{(2)}_n$ and similarly by $u^{(3)}_n$, arriving at two simultaneous equations containing $\delta\lambda_{(2)}$. Eliminating the rotation matrix elements r_{ij} in these equations results in a quadratic equation for $\delta\lambda_{(2)}$ (Chapman and Pratt, 1992) with two solutions,

$$\delta\lambda^+_{(2)} = \frac{c}{4V}(B_{22} + B_{33} + B) \tag{13}$$

and

$$\delta\lambda^-_{(2)} = \frac{c}{4V}(B_{22} + B_{33} - B), \tag{14}$$

where

$$B_{mn} = \hat{s}_i\hat{s}_\ell u^{(m)}_j u^{(n)}_k \delta a_{ijk\ell}, \tag{15}$$

V is the velocity of electromagnetic energy propagation in the unperturbed medium, c is the velocity of electromagnetic waves in a vacuum, and

$$B = \sqrt{(B_{22} - B_{33})^2 + 4B_{23}^2}. \tag{16}$$

As noted in Chapman and Pratt (1992), the perturbed velocity is a nonlinear function of the medium perturbations $\delta a_{\ell imn}$ caused by the presence of the square root given by B. Furthermore, when an isotropic medium is perturbed slightly, two velocities appear, given by equations (13) and (14). Because we are interested in the first arriving energy, we always take the higher velocity, given by equation (13).

To use equations (13) and (14) in a linearized inversion scheme, we could take one of several approaches (Červený and Jech, 1982; Jech and Pšenčík, 1989; Chapman and Pratt, 1992). If the polarizations in the perturbed medium are known, one can choose $\mathbf{u}^{(2)}$ and $\mathbf{u}^{(3)}$ to lie along the principle directions, with $B_{23} = 0$ and

$$\delta\lambda_{(n)} = \frac{cB_{nn}}{2V} \tag{17}$$

(Chapman and Pratt, 1992). Alternatively, it is possible to use the mean arrival time of the two waves, which is linear in the perturbations (Červený and Jech, 1982), such that

$$\frac{1}{2}\left(\delta\lambda^{+}_{(2)} + \delta\lambda^{-}_{(2)}\right) = \frac{c}{4V}(B_{22} + B_{33}). \tag{18}$$

Another approach is to assume that only a subset of the medium parameters is perturbed to make use of the fact that the perturbed velocity is linear in any one subset. The final approach that we discuss involves the assumption that B_{22} and B_{33} are almost equal, making $(B_{22} - B_{33})^2$ small relative to $4B_{23}^2$ in B. Then, the square root given by B may be expanded in a power series and terms of degree greater than 1 may be neglected. The result is then linear in the perturbations, such that

$$\delta\lambda^{\pm}_{(2)} = \frac{c(B_{22} + B_{33} \pm 2B_{23})}{4V}. \tag{19}$$

We now consider computations for the cross-borehole situation in which all raypaths are restricted to a single plane defined by the boreholes. In considering electromagnetic waves propagating from a transmitter in one borehole to a receiver in an adjacent borehole, a convenient choice of coordinates is

$$\begin{aligned}
\hat{\mathbf{u}}^{(1)} &= \hat{\mathbf{s}} = (s_1, 0, s_3),\\
\hat{\mathbf{u}}^{(2)} &= \hat{\mathbf{s}}^{\perp} = (-s_3, 0, s_1),\\
\hat{\mathbf{u}}^{(3)} &= \hat{\mathbf{s}} \times \hat{\mathbf{s}}^{\perp} = (0, 1, 0).
\end{aligned} \tag{20}$$

The coefficients B_{mn} now may be computed on the basis of the vectors given above and the perturbed medium parameters [perturbations of equation (4) or (9)]. Consider the parameters in the transformed coordinates in which the perturbed parameters are given by

$$\delta a_{\ell imn} = -\delta\nu_{jq} e_{i\ell j} e_{qnm}. \tag{21}$$

Then, B_{22} is given by

$$\begin{aligned}
B_{22} &= \delta a_{ijk\ell}\hat{s}_i\hat{s}_\ell\hat{s}^{\perp}_j\hat{s}^{\perp}_k\\
&= -\delta\nu_{pq} e_{jip} e_{q\ell k}\hat{s}_i\hat{s}_\ell\hat{s}^{\perp}_j\hat{s}^{\perp}_k.
\end{aligned} \tag{22}$$

Now, $e_{q\ell k}\hat{s}_\ell\hat{s}^{\perp}_k$ represents the components of $\hat{\mathbf{s}} \times \hat{\mathbf{s}}^{\perp}$, which equals $\hat{\mathbf{u}}^{(3)}$. Similarly, $e_{jip}\hat{s}_i\hat{s}^{\perp}_j$ represents $-\hat{\mathbf{u}}^{(3)}$. Therefore,

$$B_{22} = \delta\nu_{pq}\hat{u}^{(3)}_p\hat{u}^{(3)}_q \tag{23}$$

and, from equation (20), the components of $\hat{\mathbf{u}}^{(3)}$ are either 0 or 1. Similarly,

$$\begin{aligned}
B_{33} &= \delta\nu_{pq}\left(e_{pij}\hat{s}_i\hat{u}^{(3)}_j\right)\left(e_{q\ell k}\hat{s}_\ell\hat{u}^{(3)}_k\right)\\
&= \delta\nu_{pq}\hat{s}^{\perp}_p\hat{s}^{\perp}_q.
\end{aligned} \tag{24}$$

Therefore, the mean traveltime of the two waves is

$$\frac{1}{2}\left(\delta\lambda^{+}_{(2)} + \delta\lambda^{-}_{(2)}\right) = \frac{c\delta\nu_{pq}}{4V}\left(\hat{u}^{(3)}_p\hat{u}^{(3)}_q + \hat{s}^{\perp}_p\hat{s}^{\perp}_q\right). \tag{25}$$

Alternatively, if the linearization approach is undertaken,

$$\begin{aligned}
B_{23} &= \delta\nu_{pq} e_{pij} e_{q\ell k}\hat{s}_i\hat{s}_\ell\hat{s}^{\perp}_j\hat{u}^{(3)}_k\\
&= \delta\nu_{pq}\hat{u}^{(3)}_p\hat{s}^{\perp}_q
\end{aligned}$$

must be considered, and we obtain the explicit form

$$\delta\lambda_{(n)} = \frac{c\delta\nu_{pq}}{4V}\left(\hat{u}^{(3)}_p\hat{u}^{(3)}_q + 2\hat{u}^{(3)}_p\hat{s}^{\perp}_q + \hat{s}^{\perp}_p\hat{s}^{\perp}_q\right) \tag{26}$$

for equation (19). The components of the unit vectors $\hat{\mathbf{s}}$ and $\hat{\mathbf{s}}^{\perp}$ may be written in terms of trigonometric functions, since

$$\hat{\mathbf{s}} = (\cos\theta, 0, \sin\theta), \tag{27}$$

where θ is the angle that the ray makes with the x-axis. To examine the variation in the mean velocity of the two waves, which we consider in the next section, we use

$$\begin{aligned}
\frac{1}{2}\left(\delta\lambda^{+}_{(2)} + \delta\lambda^{-}_{(2)}\right) = \frac{c}{4V}\big(&\delta\nu_{22} + \delta\nu_{11}\sin^2\theta + \delta\nu_{33}\cos^2\theta\\
&+ 2\delta\nu_{13}\sin\theta\cos\theta\big).
\end{aligned} \tag{28}$$

Because we are considering a 2-D problem, the out-of-plane variation in parameters is ignored and we assume that $\delta\nu_{22}$ may be neglected. The result is an equation dependent on three parameters,

$$\frac{1}{2}\left(\delta\lambda^{+}_{(2)} + \delta\lambda^{-}_{(2)}\right) = \frac{1}{4V}[I_m + D_m\cos 2\theta + O_m\sin 2\theta], \tag{29}$$

where

$$I_m = (\delta\nu_{11} + \delta\nu_{33})/2$$

is the isotropic component of the transformed dielectric matrix,

$$D_m = (\delta\nu_{33} - \delta\nu_{11})/2$$

is the deviatory component, and

$$O_m = \delta\nu_{13}$$

is the off-diagonal component. The components of I_m, D_m, and O_m are bilinear combinations of the elements of (ϵ) and (μ). Because the transformation of the dielectric matrix $(\nu) = (\mu)^{-1}_{1/2}(\epsilon)(\mu)^{-1}_{1/2}$ is a similarity transformation, the trace of the matrix is invariant, representing the isotropic component of the dielectric matrix. For a weakly magnetic material, this component may be related directly to the isotropic component of the velocity of electromagnetic waves in the medium.

In the next section, we apply these techniques to a suite of cross-borehole experiments conducted at INEL. First, we present the analysis of a synthetic data set to discuss some of the issues involved in an inversion of radar traveltime data.

Inversion methodology and inversion of synthetic arrival times

For an illustration of the estimation of velocity anisotropy, consider Figure 1. A relatively uniform anisotropic medium (the fast direction is indicated by the black line segments in Figure 1a) is cut by a linear anisotropic low-velocity feature. The low-velocity zone may represent a fracture, a layer, or a rubble zone. The velocity anomaly consists of a velocity decrease of 0.005 m/ns with respect to a background isotropic component of 0.09 m/ns, and the anisotropy is 5% of the background isotropic value. All velocity plots related to the synthetic example represent deviations from the constant background velocity of 0.09 m/ns. A series of radar pulses is transmitted from 72 transmitters on the left through the medium to between 27 and 57 receivers on the right, for a total of 3599 source-receiver pairs. The locations of the transmitters and receivers are connected by straight lines in Figure 1b. The first-arrival times were calculated with electromagnetic ray tracing, neglecting deviations in the raypaths caused by the slight variations in materials properties. The synthetic first-arrival times, which we refer to as "observed," are shown in Figure 2 as a function of source-receiver separation. Two slopes are visible because of the two distinct velocities. Figure 2 shows the calculated velocity as a function of source-receiver angle, and there is a clear systematic variation induced by the anisotropy.

The inversion methodology is essentially identical to that applied in seismic traveltime tomography (Peterson et al., 1985; Nolet, 1987). In particular, the integral

$$\delta T = -\frac{c^2}{4}\int_{\Pi}\frac{[I_m + D_m\cos 2\theta + O_m \sin 2\theta]}{V^3}\,d\pi, \quad (30)$$

formed by the integration of the velocity perturbation in equation (29) along the raypath (π), is used to compute traveltime deviations. For computational purposes, the integral in equation (30) is discretized into a sum. This is done by subdividing the 2-D area between the boreholes into a 15×30 array of nonoverlapping cells or blocks (Figure 1b). The path of a particular electromagnetic ray through a given block is described by a straight line from the entry point of the ray to the exit point of the ray from the cell. The ray length in the cell, the ray angle through the cell, and the background velocity in the cell provide the necessary parameters for a discretized version of the integral in equation (30).

In addition to anisotropy, we solve for source and receiver static terms. Such terms are time shifts associated with sources

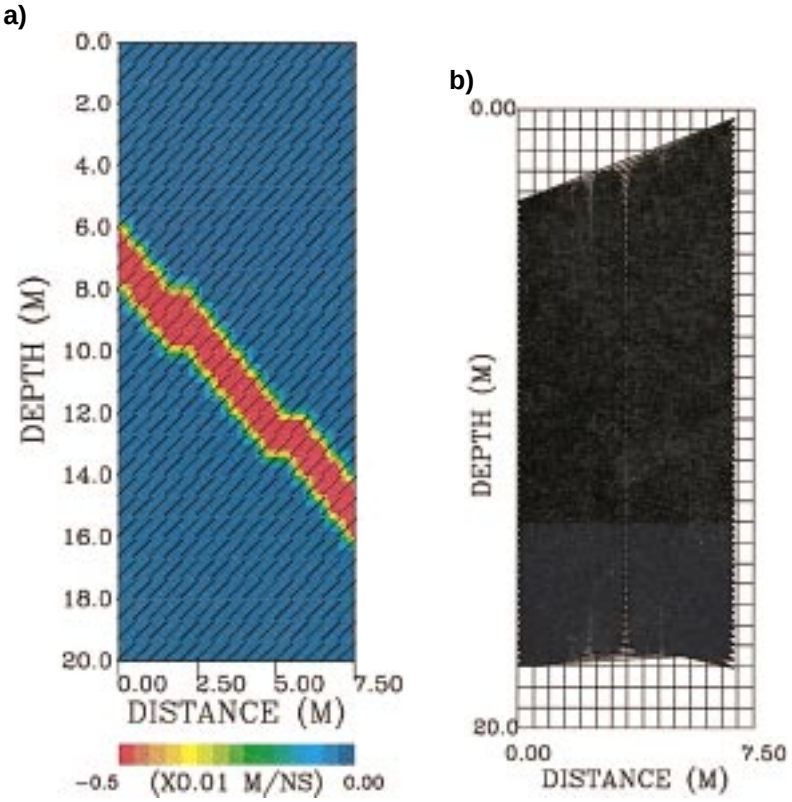

FIG. 1. (a) Radar-wave velocity model used to generate a set of synthetic first arrival times. The color scale represents deviations of velocity from a uniform background value of 0.09 m/ns. (b) Source-receiver geometry and parameterization for the synthetic test. The straight lines connect source-receiver pairs used in the synthetic crosswell experiment. The parameterization is indicated by the 15 (horizontal) $\times$ 30 (vertical) grid of rectangular cells.

and receivers and include effects of variations in borehole diameter, mislocation of the borehole, and mislocation within the borehole. Such statics can improve the results of an inversion dramatically, eliminating undesirable artifacts (Squires et al., 1992). The linearized equation for the traveltime deviation associated with the jth receiver and the ith source has the form

$$\delta t_{ij} = \sum_{k=1}^{Na} L_{ij}^{k} \delta v^{k} + \left[\frac{\partial t_{ij}}{\partial r_j}\right] \delta r_j + \left[\frac{\partial t_{ij}}{\partial s_i}\right] \delta s_i, \qquad (31)$$

where the anisotropy variations are represented by N_a cell velocities δv^k and the source and receiver statics are given by δs_i and δr_j, respectively. Equation (31) in matrix form is

$$\delta \mathbf{t} = \underset{\sim}{\mathbf{L}} \delta \mathbf{v} + \underset{\sim}{\mathbf{S}} \delta \mathbf{s} + \underset{\sim}{\mathbf{R}} \delta \mathbf{r}, \qquad (32)$$

where the velocity parameters are contained in $\delta \mathbf{v}$, the source statics are contained in $\delta \mathbf{s}$, and the receiver statics are contained in $\delta \mathbf{r}$. The coefficient matrix $\underset{\sim}{\mathbf{L}}$ consists of the parameters in equation (30), and the elements of $\underset{\sim}{\mathbf{R}}$ and $\underset{\sim}{\mathbf{S}}$ are given by $\partial t_{ij}/\partial r_j$ and $\partial t_{ij}/\partial s_j$, respectively, that is, matrices of 0's and 1's depending on whether the source/receiver is active.

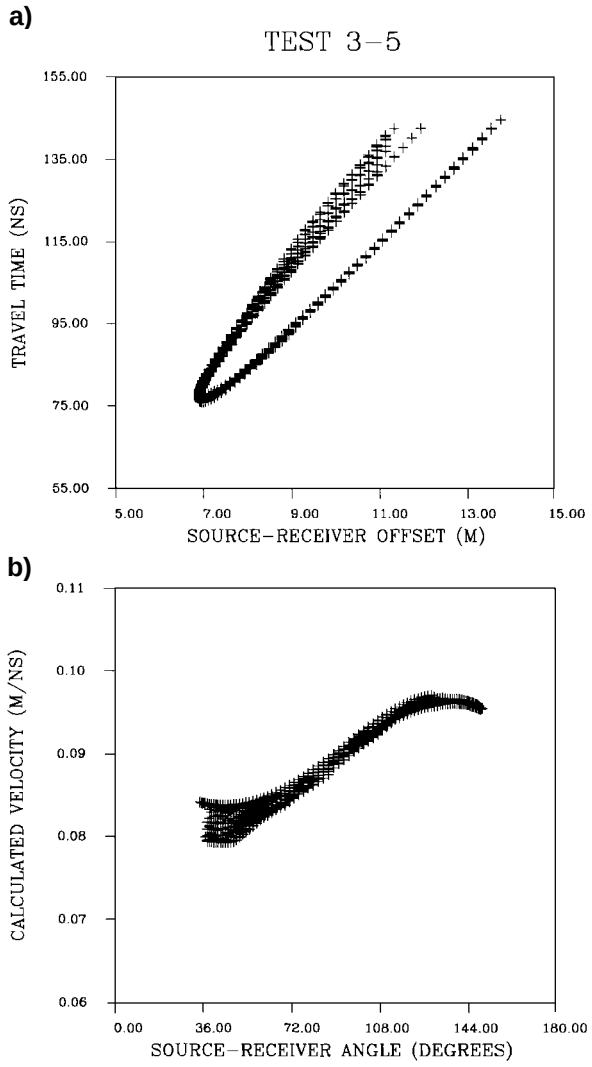

FIG. 2. (a) Traveltimes through the model shown in Figure 1 as a function of source-receiver offset. (b) Calculated velocity, based on the traveltimes in (a) and the source-receiver distance, as a function of source-receiver angle.

The velocity, source, and receiver parameters may be represented by a single vector of unknown parameters $\mathbf{x} = (\delta \mathbf{v}, \delta \mathbf{s}, \delta \mathbf{r})$. We form the residual vector between the observed arrival-time data and a predicted set of arrival times as

$$\mathbf{r}(\mathbf{x}) = \delta \mathbf{t} - \underset{\sim}{\mathbf{L}} \delta \mathbf{v} - \underset{\sim}{\mathbf{S}} \delta \mathbf{s} - \underset{\sim}{\mathbf{R}} \delta \mathbf{r}. \qquad (33)$$

The problem of finding a model that fits M arrival-time observations involves minimizing the sum of the squares of the residuals

$$\mathcal{F}(\mathbf{x}) = \sum_{i=1}^{M} r_i^2(\mathbf{x}). \qquad (34)$$

Given the 3599 arrival times and 3×450 unknown parameters, we may solve the system of equations directly, for example, using an iterative least-squares solver such as the LSQR algorithm (Paige and Saunders, 1982). However, it is clear from an examination of Figure 1b that some cells are completely unsampled but that other cells are extensively sampled by rays at many angles. Therefore, a direct solution of equation (32) is likely to be unstable in that small errors in the data might produce large changes in the solution. Therefore, we introduce regularization (Nolet, 1987) through penalty terms added to the misfit criterion. These additional terms represent model characteristics that are thought to be undesirable. For example, a rough velocity model might seem unreasonable given the averaging property of electromagnetic waves. We measure the roughness of the velocity model using a finite-difference approximation of its spatial derivatives in the plane, $\nabla^2 \delta \mathbf{v}$. In addition, extremely large-amplitude velocity variations and source and receiver terms might not be expected. One measure of model size is the sum of the squares of the N components of the model vector,

$$\mathcal{A}(\mathbf{x}) = \sum_{i=1}^{N} x_i^2 = \mathbf{x}^T \cdot \mathbf{x}. \qquad (35)$$

The penalized misfit function $\mathcal{P}(\mathbf{x})$, incorporating all of the ideas given above, is written as

$$c_d \sum_{i=1}^{M} r_i^2(\mathbf{x}) + c_r \nabla^2 \delta \mathbf{v}^T \cdot \nabla^2 \delta \mathbf{v} + c_a \mathbf{x}^T \cdot \mathbf{x}, \qquad (36)$$

where c_d, c_r, and c_a are the weighting coefficients for the data misfit, model roughness, and model norm penalty terms, respectively. Note that there are model roughness and model norm penalty terms for each anisotropy coefficient and that it is possible to penalize the anisotropy coefficients differently from the isotropic coefficients. It is the quantity $\mathcal{P}(\mathbf{x})$ that we minimize using the LSQR algorithm of Paige and Saunders (1982).

For comparison, the traveltimes (Figure 2) were inverted for an isotropic velocity structure and source and receiver static corrections. The result (Figure 3) recovers the basic feature in the model used to generate the data: a low-velocity anomaly cutting across the region between the boreholes. However, artifacts resulting from anisotropy are clearly visible in the isotropic inversion result. In particular, large-magnitude

high- and low-velocity anomalies alternate in the four corners of the region. Furthermore, the magnitude of the anomalies is three times larger than that of the isotropic component of the synthetic structure. In a more complex geology, artifacts resulting from anisotropy could obscure important features completely.

Before an inversion of actual data was attempted, we explored the trade-off between fitting the data and the size of the anisotropic component of the model, as parameterized by the model norm coefficient c_a in equation (36). That is, 50 inversions were executed at different values of c_a, and the data misfit $\mathcal{F}(\mathbf{x})$ and the model norm $\mathcal{A}(\mathbf{x})$ were noted for each inversion. Figure 4 is a plot of misfit versus model size or norm for the 50 inversions and the values of $\log(c_a)$ corresponding to each point on the trade-off curve. To balance the fit to the data and the model norm, we chose $\log(c_a) = 2.4$. The respective values for c_d and c_r were 1 and 0. The corresponding solution (Figure 5) compares quite well with the synthetic structure (Figure 1). The low-velocity anomaly is quite sharp, and the direction of maximum velocity is recovered in most of the cells. As in the isotropic case, the poorest results are in cells near the four corners because of poor angular sampling there. In conclusion, it is possible to recover anisotropic velocity structure using first-arrival times and the given source-receiver configuration. This observation is important because the source-receiver configuration used here is typical of that in the actual INEL experiments described in the next section.

IDAHO NATIONAL ENGINEERING LABORATORY CROSSWELL EXPERIMENTS

In an effort to understand fluid flow and contaminant transport in fractured basalt, scientists at the Berkeley Laboratory (BL) and INEL are collaborating in an integrated geological, hydrological, and geophysical study in the eastern Snake River

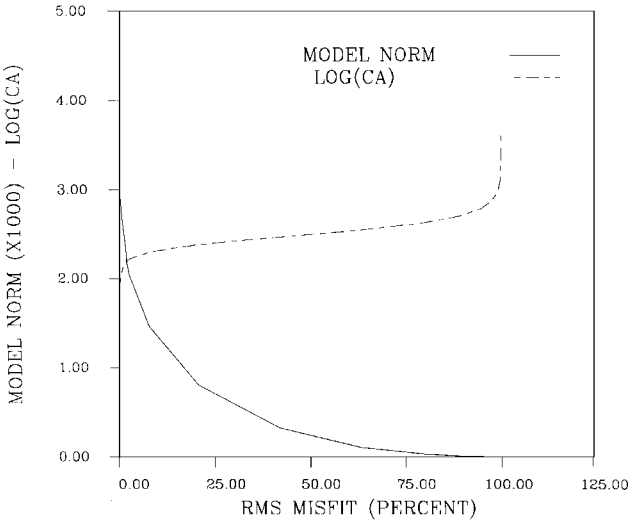

FIG. 4. Variations in root-mean-square (rms) misfit and model norm (solid line) as the model norm weighting coefficient is varied. The base 10 logarithm of the model norm weighting coefficient (dashed line) corresponds to the trade-off curve.

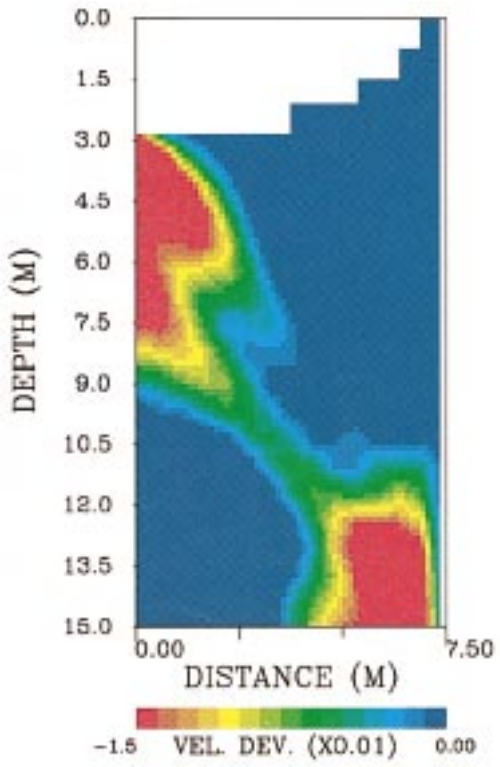

FIG. 3. Velocity variations (VEL. DEV.) from a background value of 0.09 m/ns in an isotropic inversion. Data were obtained from an LSQR inversion of the arrival times in Figure 2 and an isotropic velocity parameterization.

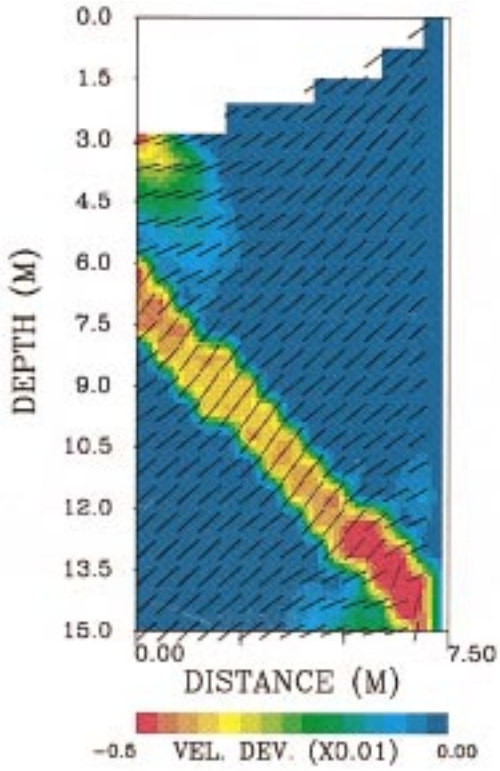

FIG. 5. Anisotropic inversion results. The velocity variations (VEL. DEV.) are with respect to a mean background value of 0.09 m/ns. The directions of maximum velocity are denoted by the straight line segments.

Plain at Box Canyon, 4.2 km south of Butte City, Idaho. This is an analog site for actual waste storage areas at INEL. One aspect of the investigations is to evaluate the potential of geophysical and hydrological methods to characterize the subsurface. Of interest is the determination of the vertical fluid flux through the area, particularly the time required for fluid to reach the underlying water table. Identifying and mapping locations of rapid downward fluid movement will allow better design of monitoring systems as well as better control of water migration and contaminant transport. In this section, we focus on the cross-borehole radar surveys conducted at Box Canyon.

The center of the study area is 30 m from an exposed cliff face that provides a comprehensive view of the subsurface geology. In addition, 17 wells, varying in depth from 12 to 22.5 m, have been drilled into the basalt (Figure 6). On the basis of cliff face mapping and borehole logs, a general geological model has been constructed. The study region encompasses two basalt flows that interfinger near the bases of many of the wells. The upper basalt is 11–12 m thick and is cut by numerous vertical fractures that result from cooling contraction. The surface of the upper basalt is covered by soil that seals all surface fractures and joints between basalt columns. Vesicular lenses 1–20 cm thick are embedded within the upper basalt; many of these are cut by horizontal fractures. At the cliff face, the contact between the two basalt flows is observed as a continuous series of rubble zones 16–19 m below the land surface. Approximately 3 m above the interface between the two flows there is a 1-m-thick fracture zone that is seen in both the boreholes and the exposed cliff face. The zone is shallowest to the north and deepens to the south and west. The implications of the site geology for crosswell radar relate to the relative importance of variations in magnetic permeability (μ), with respect to changes in the dielectric matrix or permittivity (ϵ). It appears that the strongest variations in electrical properties are associated with material contained within basalt fractures. That is, variations in properties within a given basalt flow are smaller than either variations between basalt flows or deviations induced by fractures within the basalt.

During a 7-day period, personnel from BL, Sensors and Software of Canada, and North American Exploration of Virginia conducted cross-borehole radar surveys in four well pairs at Box Canyon: II-5/II-6, II-5/II-4, II-5/II-3, II-3/II-4, (Figure 6). In addition to cross-borehole surveys, surface-to-borehole and single-well surveys were executed. The borehole radar equipment consisted of a Pulse Ekko 100 System.* The transmitter and receiver were two 100-MHz borehole antennas powered by batteries located at the surface. The transmitting antenna sends a number of radar pulses that are sensed, averaged, and stored by the receiver. For each source gather, the transmitter was fixed in depth and the receiving antenna was run down the other borehole. Then the transmitter was moved to a new depth and the sequence was repeated.

For the moment, we concentrate on well pair II-3/II-5 to compare isotropic and anisotropic inversion results. The first-arrival times were picked manually from the raw recorded waveforms. The observed traveltimes are shown in Figure 7a as a function of source-receiver separation. Although there is considerable scatter in the arrival times, two dominant slopes are evident and indicate two distinct velocities. As a rough measure of anisotropy, Figure 7b shows the calculated velocity (the source-to-receiver distance divided by the observed traveltime) as a function of source-receiver angle. For a homogeneous medium, the points would lie along a horizontal line.

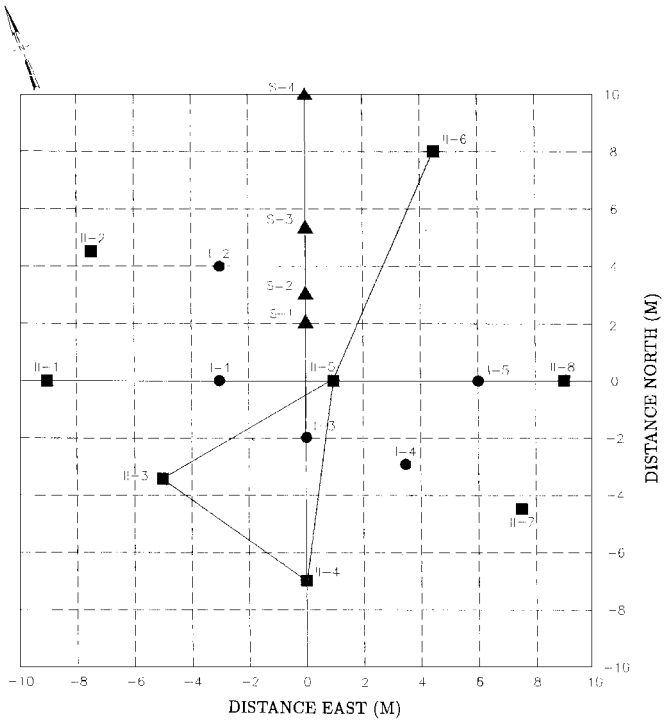

FIG. 6. Schematic map of the well locations within the Box Canyon study site. The straight line segments connect well pairs that were used for cross-borehole radar surveys.

*Trade name of Sensors and Software.

In Figure 7b, there appears to be a systematic variation as a function of angle of propagation. Note that lateral variations in velocity also may induce deviations from a horizontal line, reflecting a fundamental difficulty in distinguishing variations in anisotropy from isotropic lateral heterogeneity (Grechka and McMechan, 1995).

The region between wells II-3 and II-5 was subdivided into a 15 (horizontal) × 30 (vertical) grid of cells. The 3599 observed arrival times were used to infer variations in the velocities of each cell. All velocities shown are deviations from a mean value that was computed and subtracted from each tomogram. In the results of the isotropic inversion (Figure 8a), low velocities probably correspond to the series of rubble zones that lie between the upper and lower flows. We constructed a trade-off curve for the anisotropic inversion using a procedure similar to that described in the previous section. For this inversion and those described below, a value of $\log(c_a) = 2.4$ was used. The overall features remain intact when anisotropy is included (Figure 8b). As in the synthetic case, the level of heterogeneity observed within the isotropic component of the anisotropic inversion is about one third of the heterogeneity observed within the isotropic inversion. The image of the lower contact is sharper when anisotropy is included, and there is a hint of a subhorizontal feature at a depth of 6 m. The direction of maximum velocity, denoted by the straight line segments, is fairly constant throughout the upper basalt flow. The direction of maximum velocity may trade off with lateral heterogeneity and should be interpreted with some caution.

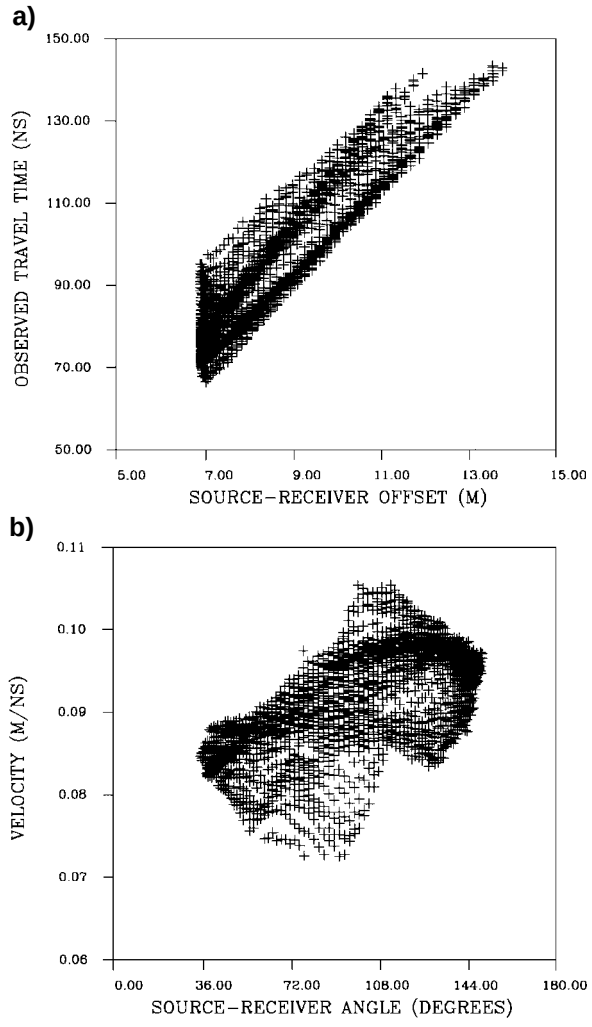

FIG. 7. (a) Observed traveltimes plotted as a function of the straight line distance between the source and the receiver for well pair II-3/II-5. (b) Calculated velocity, based on the source-receiver offset and the observed traveltimes, plotted as a function of source-receiver angle.

In Figure 9, the residuals associated with the isotropic and anisotropic inversions are compared. The upper panels show the observed versus the predicted residuals. The observed residuals are traveltime variations with respect to a homogeneous half-space. By predicted residuals, we mean the difference between a traveltime based on the LSQR model and one computed relative to the same homogeneous half-space as that used to compute the observed residuals. There is considerably less scatter when the two additional anisotropy parameters are included in the inversion. The lower panels display the predicted velocity as a function of source-receiver direction when the effects of heterogeneity (Figure 9a) and anisotropy (Figure 9b) are removed. The post–isotropic inversion residuals appear to contain a systematic variation with angle, whereas the post–anisotropic inversion residuals do not.

The remaining three cross-borehole radar surveys, II-6/II-5, II-4/II-5, and II-3/II-4, are analyzed in a similar fashion. Only anisotropic inversions were conducted on these data sets. The observed residuals are shown in Figure 10 as a function of source-receiver offset. The arrival times for surveys II-6/II-5 and II-3/II-4 lie fairly close to a single straight line of constant slope. On the other hand, the traveltimes of well pair II-4/II-5 fall along two lines with distinct slopes. When the arrival times are converted to velocity, based on the source-receiver separation, and plotted as a function of source-receiver angle, there are differences between survey II-4/II-5 data and data from the other two surveys. The calculated velocities associated with II-4/II-5 contain a strong variation as a function of source-receiver angle; those for II-6/II-5 and II-3/II-4 are not so dependent on source-receiver angle. These distinctions point to the difficulty in untangling lateral variations in isotropic velocity and lateral variations in anisotropy.

As in the inversion of the II-3/II-5 residuals, we use an LSQR algorithm to conduct a regularized least-squares inversion. The norm weighting coefficient c_a is identical to that used previously. In 40 iterations, the LSQR algorithm converged, producing a set of anisotropy parameters and source and receiver static terms. The postinversion residuals for the three surveys (Figure 11) agree quite well with the observed traveltime residuals. When the residuals are plotted as a function of angle, corrected for anisotropy and lateral heterogeneity, there is no significant variation with source-receiver angle.

Taken separately, the results obtained by the inversion of INEL cross-borehole radar traveltimes are quite encouraging. However, because the well pairs are contiguous (Figure 6), they may be most profitably examined together. Consider pairs II-6/II-5 and II-5/II-4, which form a kinked line running north-northeast to south-southwest. The tomograms agree quite well. A subhorizontal low-velocity zone observed at 6 m in II-6/II-5 continues across II-5/II-4 (Figure 12). There is also a prominent low-velocity anomaly associated with the rubble zones separating the two basalt units, below a depth of about 11 m. Unfortunately, the ray coverage degrades near this edge, and

the lower anomaly is not well constrained. Furthermore, the upper-lower basalt flow boundary is continuous across the two models, deepening to the south, as observed in outcrops and cores. The results are similar for pairs II-6/II-5 and II-5/II-3.

If we unfold the triangle formed by the three tomograms II-5/II-3, II-3/II-4, and II-4/II-5 (Figure 13), the continuity of structure is clearly visible, particularly the low-velocity anomalies between 6 and 8 m. Tomograms for well pairs II-4/II-5 and II-3/II-4 also contain low velocities between 6 and 9 m. Section II-4/II-5 samples the lower flow unit and rubble zone, which appear as low-velocity anomalies. The anisotropy is not shown in Figure 13 because of the significantly different azimuths of the well pair planes. We do not expect the anisotropy in the various planes to agree if the planes are oriented in dramatically different directions. However, because each tomogram produces an estimate of apparent anisotropy restricted to that particular plane, we may estimate the actual direction of maximum velocity. Using the panels for well pairs II-5/II-3, II-3/II-4, and II-4/II-5, we calculate that the direction of maximum velocity dips 56° along an azimuth of 245°. This direction follows the structural trend in the region: The major flow boundary dips to the south and west. The agreement between the isotropic velocity structure for distinct and uncoupled inversions gives us confidence that we are imaging actual geological features.

CONCLUSIONS

In seismology, anisotropy is well documented and is now accounted for in crosswell tomographic inversions (Chapman and Pratt, 1992). We have shown that similar procedures can be applied to electromagnetic wave propagation, particularly in crosswell radar tomography. Including anisotropy when it is unnecessary does little harm if damping and smoothing penalties are incorporated into the inversion. However, if anisotropy is present and is not accounted for, a bias that can obscure important structures may result. Therefore, the safest strategy is to include anisotropy terms in the inversion and to examine the trade-off between fitting the data and the anisotropy magnitude.

The approach that we have taken assumes weak anisotropy and relies on perturbation techniques to linearize the problem. In our application, we have neglected deviations in the raypaths from those in our initial homogeneous structure. There is a potential trade-off between ray deviations from the straight lines used here and anisotropy coefficients that we have not addressed. That is, the straight-ray assumption is equivalent to assuming both nearly homogeneous velocities and nearly isotropic velocities. These effects could be more important in GPR than in seismology because the velocity variations are potentially much larger. As shown above, the linearized approach

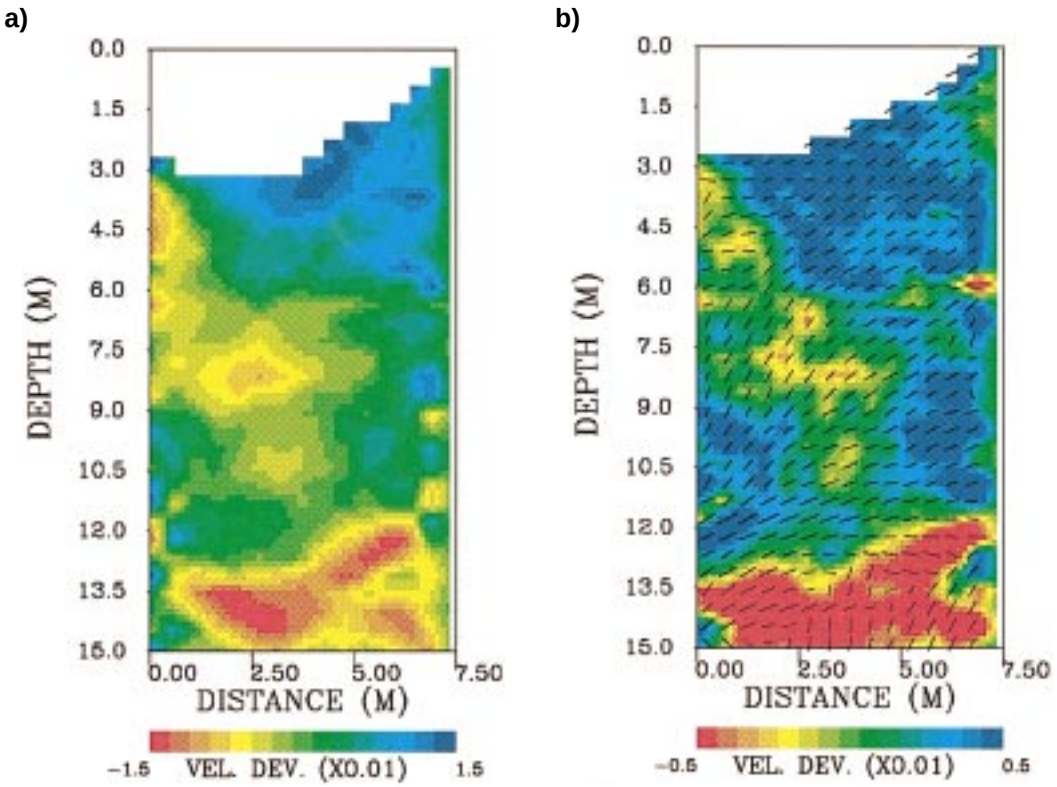

FIG. 8. (a) Isotropic inversion results for well pair II-3/II-5. Data were obtained by an LSQR inversion of the observed traveltimes shown in Figure 7, assuming the velocity is isotropic. The units are meters per nanosecond. Variations in velocity (VEL. DEV.) from a mean background value of 0.09 m/ns are shown. The lowest velocities, indicated by red-yellow colors, are found at the bottom of the region. (b) Anisotropic inversion results. Data were obtained by an LSQR inversion of the observed traveltimes, assuming that the velocity is a function of angle from the vertical. The line segments depict the direction of maximum velocity.

has proven very effective in interpreting the GPR first arrival times gathered in the INEL surveys. Several alternatives to the linearized one-step inversion are suggested by derivations presented in this paper. An iterative approach in which the perturbation linearization becomes one step in a nonlinear inversion algorithm could be adopted. At each step, rays would be traced through the model and the resulting raypaths would be used in the integral in equation (30).

An alternative to ray tracing is to solve the eikonal equation, given in the Appendix by equation (A-8), directly for the wavefronts, as has been done for seismic wave propagation in anisotropic media (Eaton, 1993). A finite-difference technique is used to compute the gradient of the penalized misfit function with respect to the velocity parameters [equation (36)]. Then, an iterative nonlinear optimization program is used to minimize the penalized misfit. This approach has worked well in treating the isotropic nonlinear seismic traveltime inverse problem (Vasco, 1995). We have incorporated an isotropic finite-difference code into a nonlinear, conjugate-gradient-based radar traveltime inversion program (Vasco, 1995). That is, we numerically solve the eikonal equation (A-8) for isotropic dielectric and magnetic permeability matrices, as has been done in seismology for seismic velocity (Vidale, 1988; Podvin and Lecomte, 1991). To estimate the effects of refraction on our results, we have inverted our radar data using both the linearized straight-ray approach and a fully nonlinear but isotropic approach. The results are similar for the two techniques, and the major features are present in both inversions. For example, tomograms resulting from the linear and nonlinear algorithms are shown in Figure 14 for well pair II-6/II-5. Both tomograms contain a subhorizontal low-velocity zone at around 5–6 m. In addition, a low-velocity basement is seen dipping to the right (southwest). The agreement between the inversion results is significant, especially given the differing parameterizations (isotropic/anisotropic). The low-velocity anomaly associated with the rubble zone and the lower basalt flow is larger in the conjugate-gradient solution. However, this feature lies at the lowermost edge of the tomograms and is not as well resolved as the interior velocity variations. In particular, anomalies in poorly resolved areas are sensitive to

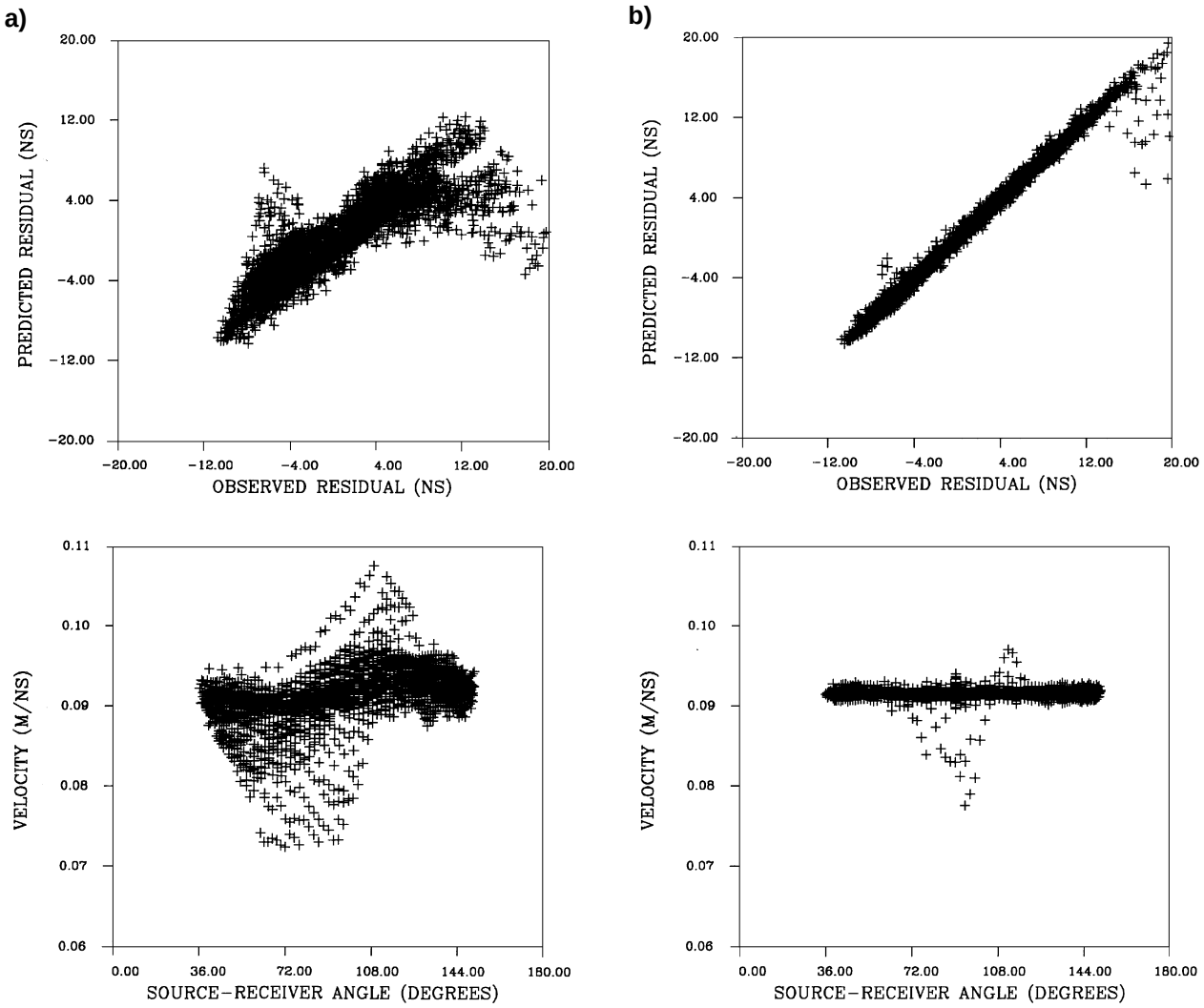

FIG. 9. (a) Isotropic inversion for well pair II-3/II-5. Observed traveltime residuals versus predicted traveltime residuals and calculated velocity as a function of source-receiver angle are shown. Both the observed and the predicted residuals are traveltime deviations with respect to arrival times calculated with a homogeneous half-space. (b) Anisotropic inversion. Observed traveltime residuals versus predicted travel time residuals and calculated velocity as a function of source-receiver angle are shown.

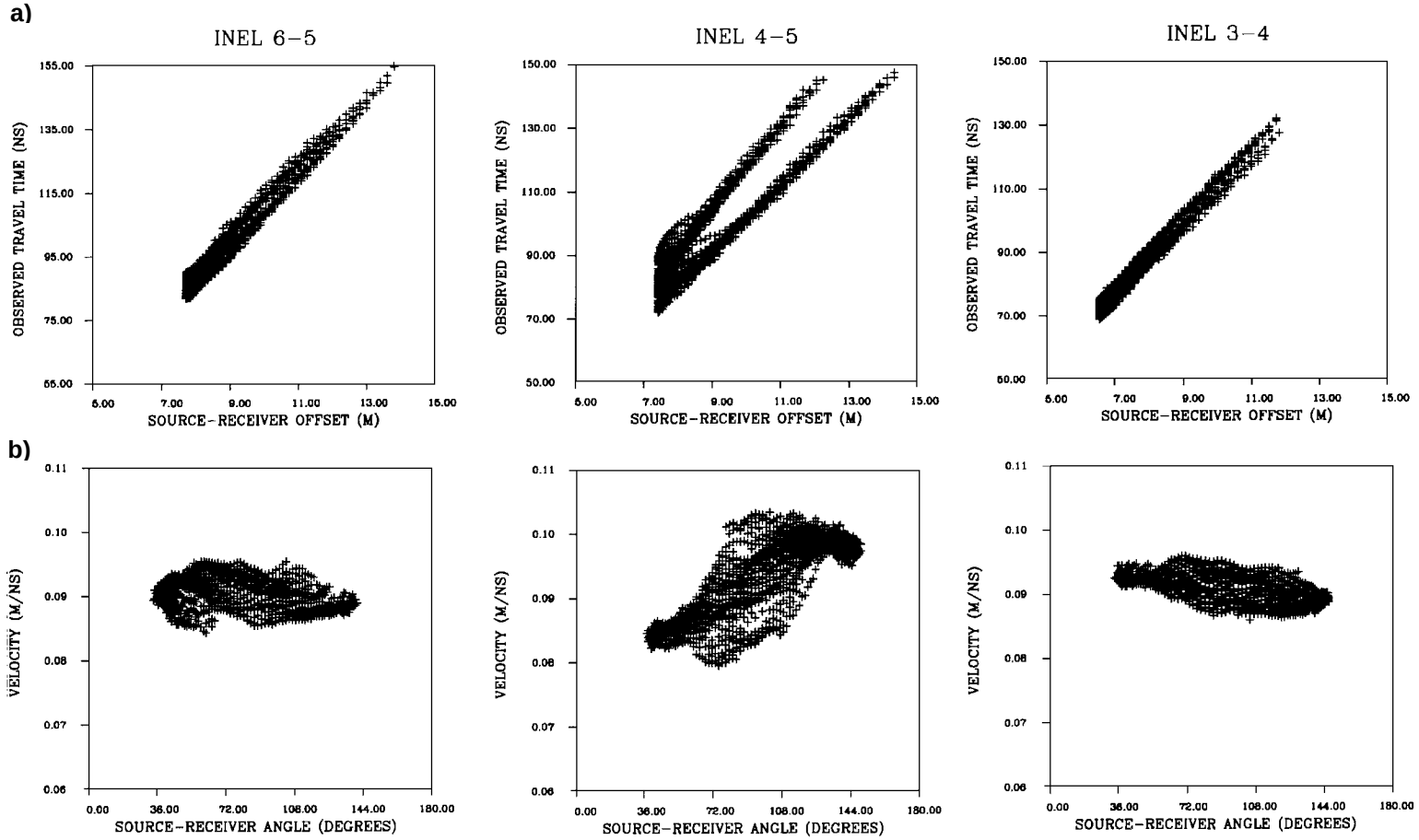

FIG. 10. (a) Observed traveltime residuals as a function of source-receiver offset for the well pairs II-6/II-5, II-4/II-5, and II-3/II-4. (b) Calculated velocity as a function of source-receiver angle for the corresponding well pairs.

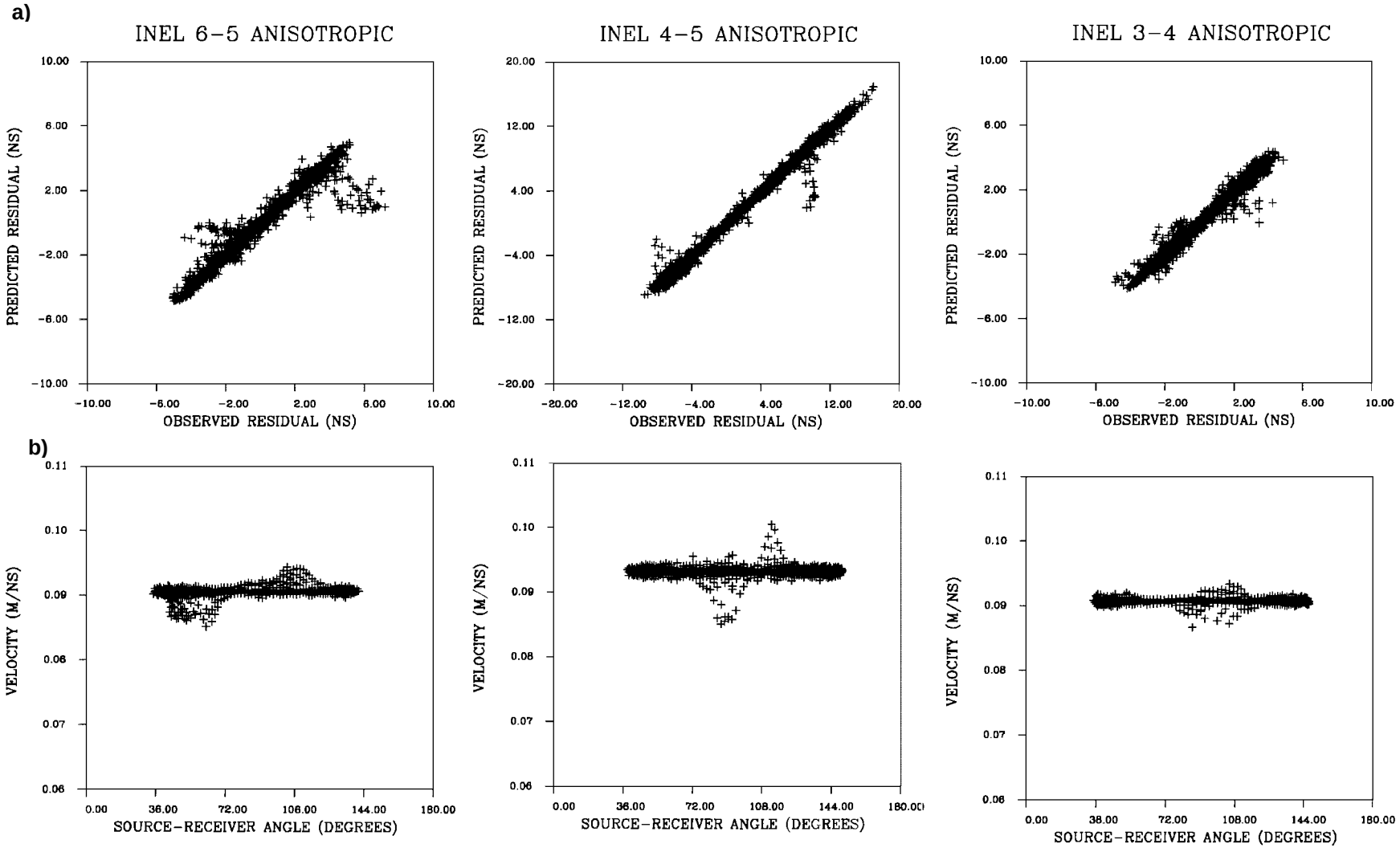

FIG. 11. (a) Observed travel time residuals versus predicted travel time residuals. (b) Calculated velocity as a function of source-receiver angle.

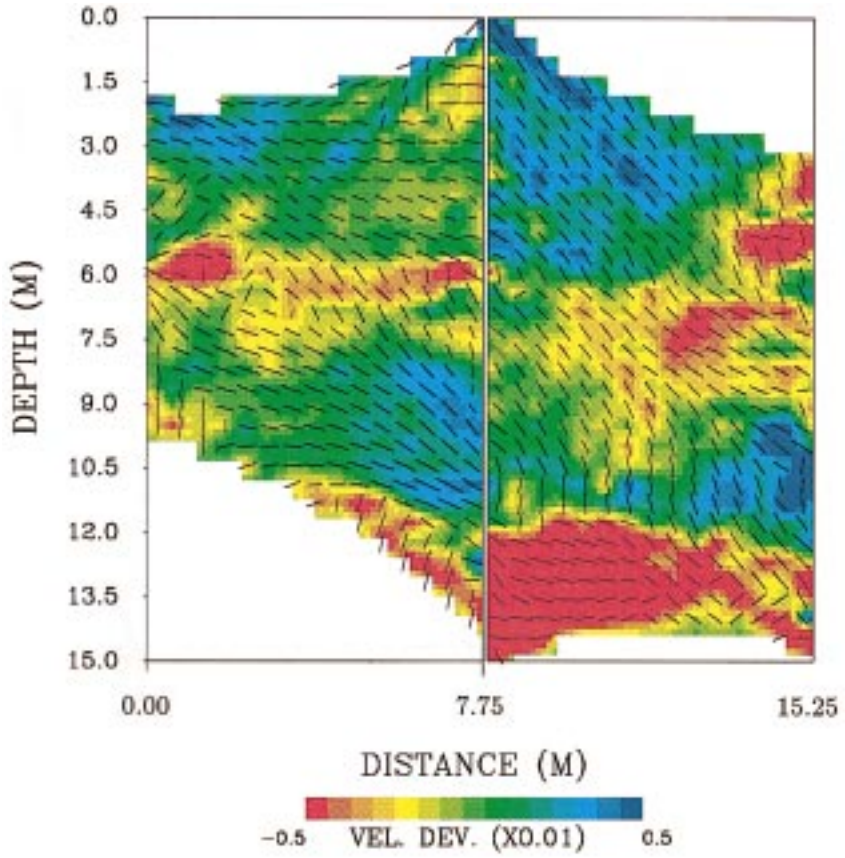

FIG. 12. Anisotropic inversion results for well pairs II-6/II-5 and II-5/II-4. The velocity variations (VEL. DEV.) are with respect to a background value of 0.09 m/ns. The line segments point in the directions of maximum velocity.

the damping and smoothing used to regularize the inversions. In the future, we would like to compare a fully nonlinear inversion for anisotropy variations with our linearized approach.

Finally, we wish to emphasize the importance of source and receiver static corrections. Although their importance was not explored here, inversions were attempted with and without source-receiver static terms. When static terms were not included as unknowns, numerous artifacts obscured important structures. We found that source-receiver static terms often can be as important as or even more important than anisotropy terms. Since they are relatively simple to include, static terms should be present in all tomographic inversions.

ACKNOWLEDGMENTS

This work was supported by the Assistant Secretary for Environmental Restoration and Waste Management, Office of Technology Development, and Director, Office of Energy Research, Office of Basic Energy Sciences, Engineering and Geosciences Division, U.S. Department of Energy, under Contract No. DE-AC03-76SF00098. We acknowledge Kenneth Williams for his contribution in acquiring the excellent GPR data at INEL.

REFERENCES

Aki, K., and Richards, P. G., 1980, Quantitative seismology: W. H. Freeman & Co.

Al Hagrey, S. A., 1994, Electric study of fracture anisotropy at Falkenberg, Germany: Geophysics, **59**, 881–888.

Backus, G. E., 1962, Long-wave elastic anisotropy produced by horizontal layering: J. Geophys. Res., **67**, 4427–4440.

Berryman, J. G., 1979, Long-wave elastic anisotropy in transversely isotropic media: Geophysics, **44**, 896–917.

Bevan, B., 1991, The search for graves: Geophysics, **56**, 1310–1319.

Born, M., and Wolf, E., 1970, Principles of optics: Pergamon Press, Inc.

Červeńy, V., and Jech, J., 1982, Linearized solutions of kinematic problems of seismic body waves in inhomogeneous slightly anisotropic media: J. Geophys., **51**, 96–104.

Chapman, C. H., and Pratt, R. G., 1992, Traveltime tomography in anisotropic media—I. Theory: Geophys. J. Internat., **109**, 1–19.

Daniels, J., 1988, Locating caves, tunnels, and mines: The Leading Edge, **7**, No. 3, 32–37.

Davis, J. L., and Annan, A. P., 1989, Ground penetrating radar for high-resolution mapping of soil and rock stratigraphy: Geophys. Prosp., **37**, 531–551.

Eaton, D. W. S., 1993, Finite difference traveltime calculation for anisotropic media: Geophys. J. Internat., **114**, 273–280.

Fisher, E., McMechan, G. A., and Annan, A. P., 1992, Acquisition and processing of wide-aperture ground-penetrating radar data: Geophysics, **57**, 495–504.

Golub, G. H., and Van Loan, C. F., 1989, Matrix computations: Johns Hopkins Univ. Press.

Goodman, D., 1994, Ground-penetrating radar simulation in engineering and archaeology: Geophysics, **59**, 224–232.

Grechka, V. Y., and McMechan, G. A., 1995, Anisotropy and non-linear polarization of body waves in exponentially heterogeneous media: Geophys. J. Internat., **123**, 959–965.

Jech, J., and Pšenčík, I., 1989, First-order perturbation method for anisotropic media: Geophys. J. Internat., **99**, 369–376.

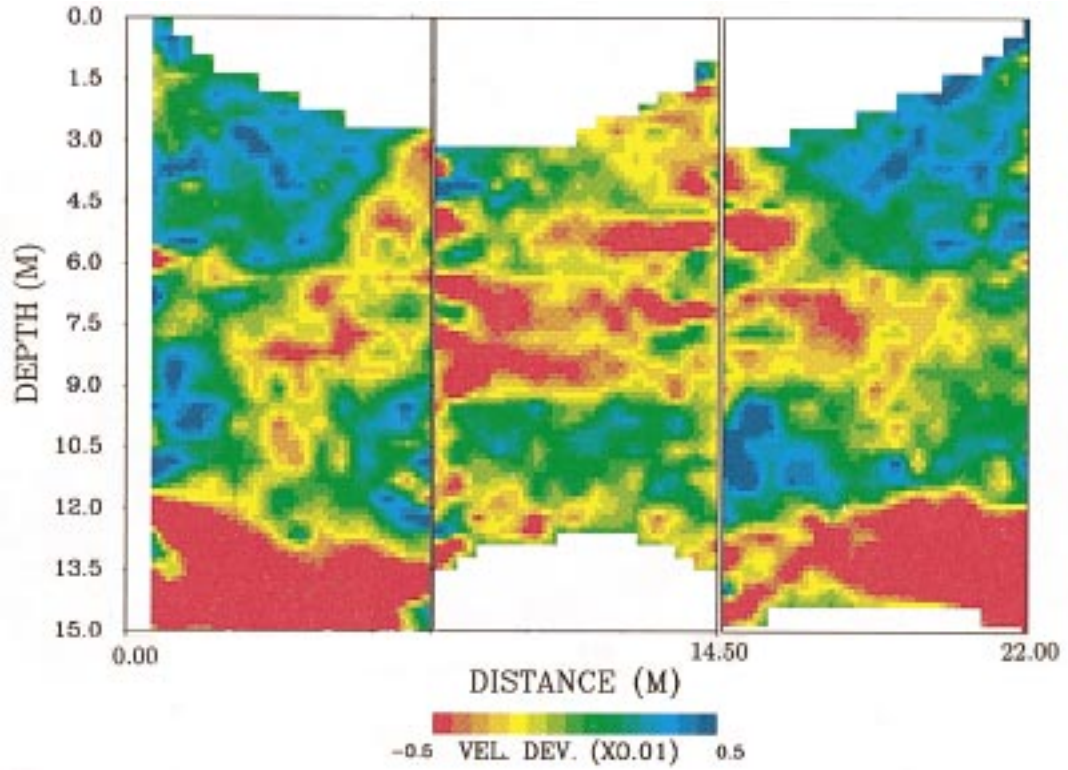

FIG. 13. Anisotropic inversion results for well pairs II-5/II-3, II-3/II-4, and II-4/II-5. The velocity variations (VEL. DEV.) are with respect to a background value of 0.09 m/ns.

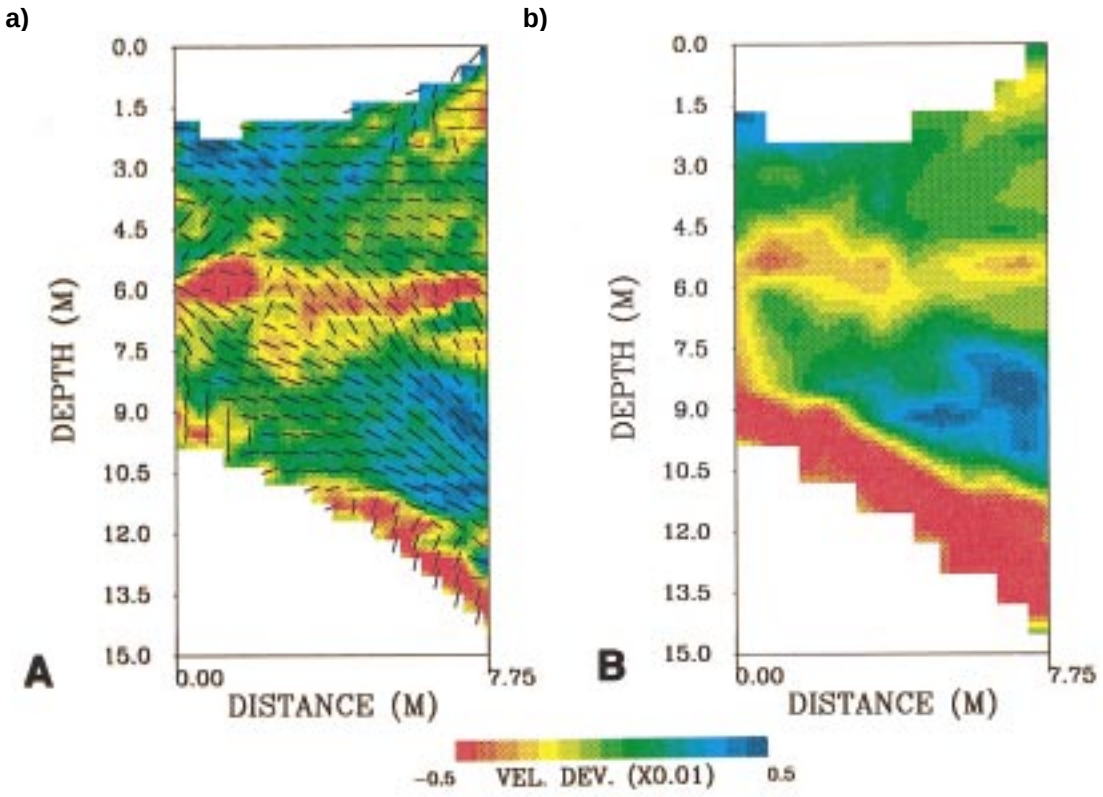

FIG. 14. Tomograms for well pair II-6/II-5 produced by two different inversion algorithms. (a) Results from a linearized straight-ray inversion for variations in anisotropy. (b) Nonlinear (conjugate-gradient) inversion for isotropic velocity structure with an eikonal equation approach [equation (A-8)] to compute the first arrival times. VEL. DEV. = Velocity deviations.

Keller, H. B., 1968, Numerical methods for two-point boundary value problems: Blaisdell.
Kline, M., and Kay, I. W., 1965, Electromagnetic theory and geometrical optics: John Wiley & Sons, Inc.
Leary, P. C., Crampin, S., and McEvilly, T. V., 1990, Seismic fracture anisotropy in the Earth's crust: An overview: J. Geophys. Res., **95**, 11 105–11 114.
Lee, K. H., and Xie, G., 1993, A new approach to imaging with low-frequency electromagnetic fields: Geophysics, **58**, 780–796.
Lee, S., McMechan, G. A., and Aiken, C. L. V., 1987, Phase-field imaging: The electromagnetic equivalent of seismic migration: Geophysics, **52**, 678–693.
Lipson, S. G., and Lipson, H., 1981, Optical physics: Cambridge Univ. Press.
Luneburg, R. K., 1966, Mathematical theory of optics: Univ. of California Press.
Nekut, A. G., 1994, Electromagnetic ray-tracing tomography: Geophysics, **59**, 371–377.
Nolet, G., 1987, Seismic wave propagation and seismic tomography, *in* G. Nolet, Ed., Seismic tomography: D. Reidel Publ. Co., 1–23.
Olsson, O., Falk, L., Forslund, O., Lundmark, L., and Sandberg, E., 1987, Crosshole investigations—Results from borehole radar investigations: Stripa Project Technical Report 87-11SKB.
Paige, C. C., and Saunders, M. A., 1982, LSQR: An algorithm for sparse linear equations and sparse linear systems: ACM Trans. Math. Software, **8**, 195–209.
Peterson, J. E., Paulsson, B. N. P., and McEvilly, T. V., 1985, Applications of algebraic reconstruction techniques to crosshole seismic data: Geophysics, **50**, 1566–1580.
Podvin, P., and Lecomte, I., 1991, Finite difference computation of traveltimes in very contrasted velocity models: A massively parallel approach and its associated tools: Geophys. J. Internat., **105**, 271–284.
Sokolnikoff, I. S., 1964, Tensor analysis: John Wiley & Sons, Inc.
Squires, L. J., Blakeslee, S. M., and Stoffa, P. L., 1992, The effects of statics on tomographic velocity reconstructions: Geophysics, **57**, 353–362.
Stewart, R., 1988, An algebraic reconstruction technique for weakly anisotropic velocity: Geophysics, **53**, 1613–1615.
Stewart, R., and Unterberger, R. R., 1976, Seeing through rock salt with radar: Geophysics, **41**, 123–132.
Thomsen, L., 1986, Weak elastic anisotropy: Geophysics, **51**, 1954–1966.
Tillard, S., 1994, Radar experiments in isotropic and anisotropic geological formations (granite and schists): Geophys. Prosp., **42**, 615–636.
Ulriksen, C. P. F., 1982, Application of impulse radar to civil engineering: Ph.D. thesis, Univ. of Technology, Lund, Sweden.
Vasco, D. W., 1995, A transformational approach to geophysical inverse problems: Geophys. J. Internat., **123**, 183–212.
Vidale, J., 1988. Finite difference calculation of travel times: Bull., Seis. Soc. Am., **78**, 2062–2076.

APPENDIX

ELECTROMAGNETIC RAY SERIES

In this Appendix, we discuss the propagation of discontinuities in the electric $\mathbf{E}(x, y, z, t)$ and magnetic $\mathbf{H}(x, y, z, t)$ fields as functions of time t and space (x, y, z). The approach is that of Kline and Kay (1965), which we believe provides an extremely useful methodology for treating the problem of electromagnetic wave propagation in the earth. Consider Maxwell's equations,

$$\begin{aligned} \operatorname{curl}\mathbf{H} &= \frac{1}{c}\mathbf{D}_t + \frac{4\pi}{c}\mathbf{J}, \\ \operatorname{curl}\mathbf{E} &= -\frac{1}{c}\mathbf{B}_t, \\ \operatorname{div}\left(\mathbf{J} + \frac{1}{4\pi}\mathbf{D}_t\right) &= 0, \\ \operatorname{div}\mathbf{B} &= 0, \end{aligned} \tag{A-1}$$

where $\mathbf{D}$ denotes the dielectric displacement vector, $\mathbf{B}$ denotes the magnetic induction vector (magnetic flux density), $\mathbf{J}$ denotes the current density vector, and c denotes the speed of light. The subscript t represents the time derivative of the respective vector. Several of the vector fields in equation (A-1) are linearly related, such that

$$\begin{aligned} \mathbf{D} &= (\epsilon)\mathbf{E}, \\ \mathbf{B} &= (\mu)\mathbf{H}, \\ \mathbf{J} &= (\sigma)\mathbf{E} + \frac{1}{4\pi}\mathbf{F}_t, \end{aligned} \tag{A-2}$$

where (ϵ), (μ), (σ) are the dielectic matrix, the magnetic permeability matrix, and the conductivity matrix, respectively, and $\mathbf{F}_t$ is the time rate of change of the source vector.

Consider a point (x_0, y_0, z_0) in space at which the electric $\mathbf{E}(x_0, y_0, z_0, t)$ and magnetic $\mathbf{H}(x_0, y_0, z_0, t)$ fields are initially zero. At a particular time, e.g., t_0, both fields have some finite value. Hence, $\mathbf{E}$ may be expressed as a power series with $t - t_0$, which may be used to represent solutions of Maxwell's equations (Kline and Kay, 1965). Geometric optic approximations are obtained from the first terms of these expansions. Note that for sufficiently long times or low enough frequencies, the power series expansion, which is an asymptotic series, diverges.

Because Maxwell's equations as given above define a system of first-order hyperbolic partial differential equations, some degree of continuity is required for $\mathbf{E}$ and $\mathbf{H}$. Since we intend to work with discontinuous solutions, an alternative form, based on an integral formulation of Maxwell's equations, is necessary. The set of points in space-time at which the discontinuity in $\mathbf{E}$ and $\mathbf{H}$ exists is denoted by $\phi(x, y, z, t)$. If the time derivative of $\phi(x, y, z, t)$ does not vanish, the equation $\phi(x, y, z, t) = 0$ for the discontinuity may be solved explicitly for t as $\psi(x, y, z) = ct$, where $\psi(x, y, z)$ is a function containing only spatial terms. Thus, $\phi(x, y, z, t)$ may be written in the form

$$\phi(x, y, z, t) = \psi(x, y, z) - ct. \tag{A-3}$$

The derivation of an integral formulation incorporating the space-time hypersurface $\phi(x, y, z, t)$ is given in Kline and Kay (1965) and will not be repeated here. The resulting system of equations is

$$\begin{aligned} \nabla\phi \times [\mathbf{H}] - \frac{\phi_t}{c}[\mathbf{D}] - \frac{\phi_t}{c}[\mathbf{F}] &= 0, \\ \nabla\phi \times [\mathbf{E}] + \frac{\phi_t}{c}[\mathbf{B}] &= 0, \\ \nabla\phi \times \left([\mathbf{J}] + \frac{1}{4\pi}[\mathbf{D}_t]\right) &= 0, \\ \nabla\phi \times [\mathbf{B}] &= 0, \end{aligned} \tag{A-4}$$

where the brackets denote the discontinuous change in the enclosed vector at time $t = \psi(x, y, z)/c$. Physically, the reason that (σ) does not appear in equation (A-4) is that, to first order, it has no influence on the geometry of the wavefronts and rays or the kinematic properties of the fields.

Wavefronts and the eikonal equation

Consider an electromagnetic disturbance propagating from a source in an anisotropic medium. At a time t_0, the space-time hypersurface $\phi(x, y, z, t)$ separates the region for which **E** and **H** are zero from the hypervolume over which they have finite values. The values of **E** and **H** when hypersurface $\phi(x, y, z, t) = 0$ are denoted by

$$\begin{aligned} \mathbf{E}^* &= \mathbf{E}\left(x, y, z, \frac{\psi}{c}\right), \\ \mathbf{H}^* &= \mathbf{H}\left(x, y, z, \frac{\psi}{c}\right), \end{aligned} \tag{A-5}$$

and similarly for $\mathbf{D}^*$ and $\mathbf{B}^*$. These two definitions may be substituted into the first two expressions of equation (A-4), noting that $\phi(x, y, z, t) = \psi(x, y, z) - ct$ and supposing that $\mathbf{F}(x, y, z, t)$ is continuous, to yield

$$\begin{aligned} \nabla\psi \times \mathbf{H}^* + \mathbf{D}^* &= 0, \\ \nabla\psi \times \mathbf{E}^* - \mathbf{B}^* &= 0. \end{aligned} \tag{A-6}$$

The wavefront is characterized by $\psi(x, y, z) - ct$. The velocity in the direction orthogonal to the wavefront is the velocity in the direction of $\nabla\psi$. We denote this direction by the vector $\mathbf{p} = \nabla\psi$. To compute the wavefronts, consider equation (A-6) and make the substitutions $\mathbf{p} = \nabla\psi$, $\mathbf{D}^* = (\epsilon)\mathbf{E}^*$, and $\mathbf{B}^* = (\mu)\mathbf{H}^*$. The result is six homogeneous linear equations for the components of $\mathbf{E}^*$ and $\mathbf{H}^*$,

$$\begin{aligned} (\epsilon)\mathbf{E}^* + \mathbf{p} \times \mathbf{H}^* &= 0 \\ -\mathbf{p} \times \mathbf{E}^* + (\mu)\mathbf{H}^* &= 0. \end{aligned} \tag{A-7}$$

For the linear system to have a nontrivial solution, the determinant of the coefficient matrix must vanish. Written in terms of the components of the vectors and matrices, this determinant is

$$\det(\epsilon_{ij}\mu_{jk} + e_{imj}e_{j\ell k}p_m p_\ell), \tag{A-8}$$

where the subscripts are values 1, 2, 3 corresponding to the x, y, z components and e_{ijk} denotes the pseudotensor that is 1 under an even permutation of indices, -1 under an odd permutation of indices, and 0 for any repetition of indices (Sokolnikoff, 1964). The summation convention of Einstein, in which any pair of identical indices denotes a summation over those indices, is invoked. Equation (A-8) corresponds to the eikonal equation for anisotropic media (Kline and Kay, 1965; Born and Wolf, 1970) and represents a scalar partial differential equation for the wavefronts when written in terms of the components of $\psi(x, y, z)$. As such, it may be solved most generally by a finite-difference technique, as has been done in seismology (Vidale, 1988; Podvin and Lecomte, 1991; Eaton, 1993).

Electromagnetic rays in anisotropic media

The flow of energy in an anisotropic medium is not necessarily parallel to **p** but is given by the vector

$$\mathbf{s} = \frac{\mathbf{E}^* \times \mathbf{H}^*}{4\pi W}, \tag{A-9}$$

where W is the electromagnetic energy density (Kline and Kay, 1965). To construct raypaths in an inhomogeneous anisotropic medium, we follow an approach similar to that adopted in the derivation of the eikonal equation. First, two equations equivalent to equation (A-7) may be derived by a formal exchange of vectors, noting that $\mathbf{D}^* = (\epsilon)\mathbf{E}^*$ and $\mathbf{B}^* = (\mu)\mathbf{H}^*$:

$$\begin{aligned} \mathbf{D}^* + (\epsilon)\mathbf{s} \times \mathbf{B}^* &= 0, \\ (\mu)\mathbf{s} \times \mathbf{D}^* - \mathbf{B} &= 0. \end{aligned} \tag{A-10}$$

Kline and Kay (1965) derived the six equations required for numerical ray tracing. Solutions for the combined system of equations may be found by any available technique for solving two-point boundary value problems (Keller, 1968).